the same weighing scheme as described for the study of $\Delta G°_i$ vs. T. For a_i the following values are found: $a_1 = 19 \pm 2$ kJ mol^{-1}, $a_2 = 59 \pm 6$ kJ mol^{-1}. For b_i, we have $b_1 = 20 \pm 3$ J K^{-1} mol^{-1} and $b_2 = -133 \pm 12$ J K^{-1} mol^{-1}. The parameters, referring to the same standard state as $\Delta H°_i$ and $\Delta S°_i$, are given within 95% confidence limits.

Obviously, the positive value of b_1 cannot be explained by the presence of two different solvent cations, since the modified theory by Bombi and Sacchetto[19] predicts $(\partial(\Delta A_1)/\partial T)_Z \leq 0$. In the present case it seems more reasonable to adopt the view that $-b_1 = (\partial(-\Delta A_1)/\partial T)_{Z=5}$ largely expresses a change in internal entropy (ΔS_{int}) of the polyatomic ions exchanging on the anion sublattice of the melt. Actually $\Delta S_{int} = -20$ J K^{-1} mol^{-1} appears to be of a more reasonable order of magnitude than $\Delta S_{int} = 80$ J K^{-1} mol^{-1}, which can be calculated (with $Z = 5$) for Ag^+–CN^- association in 1:1 (K,Na)NO_3 melts by use of data given by Manning and Blander.[21] This comparison is made here, since the study of Manning and Blander constituted the only source of information on univalent polyatomic ligand behavior in nitrate melts prior to the present work. As for the second step of association (eq 11) the large negative value of b_2 seems to be inconsistent with both "mixed solvent" and "internal entropy" explanations. For reasons already mentioned in the discussion of $\Delta H°_2$ and $\Delta S°_2$ it may also be seriously questioned if the basic quasi-lattice assumptions do hold at the attachment of a second NO_2^- to $AgNO_2$. Finally it is to be stressed that too much emphasis should not be put on the absolute values of a_i and b_i since they are influenced by the choice of Z.

(21) D. L. Manning and M. Blander, *Inorg. Chem.*, **1**, 594 (1962).

Concluding Remarks. The ability of nitrite ion to form metal complexes in nitrate melts as in aqueous solutions is clearly demonstrated. A definite conclusion about the coordination mode (nitro or nitrito) cannot be made, however, until more detailed information is available. The effects of size, charge, and chemical character of the central atom of the ligand on the thermodynamics of metal complexation with oxoanions in melts should be known. The previously cited works by Sacchetto and others[17,18] give some insight into these problems, and more information is hopefully to be gained from thermodynamic studies of a number of pertinent systems, which are in progress at our laboratory.

Acknowledgment. Experimental assistance by Miss Katrin Karlsson and Miss Kristina Andersson is gratefully acknowledged. This study has been supported by a grant from the Swedish Natural Science Research Council.

Registry No. $Ag(NO_2)_2^-$, 35772-22-6; $AgNO_2$, 7783-99-5; KNO_3, 7757-79-1; $NaNO_3$, 7631-99-4; $AgNO_3$, 7761-88-8; $NaNO_2$, 7632-00-0.

Supplementary Material Available: Table IV, giving experimental data C_{Ag}, $C_{NO_2^-}$, and $(E_0 - E_c)$ and calculated $C_{Ag}/[Ag^+]$ and $[NO_2^-]$ for all investigated melts (8 pages). Ordering information is given on any current masthead page.

Contribution from the Department of Applied Chemistry, Faculty of Engineering, and the Institute of Scientific and Industrial Research, Osaka University, Yamadakami, Suita-Shi, Osaka-Fu 565, Japan

High-Pressure Synthesis, Characterization, and Properties of Europium(II) Metaborate and Europium(II)-Activated Strontium and Calcium Metaborates

KEN-ICHI MACHIDA, GIN-YA ADACHI,* JIRO SHIOKAWA, MASAHIKO SHIMADA, and MITSUE KOIZUMI

Received August 14, 1979

High-pressure syntheses and characterization by magnetic susceptibility and luminescence measurements were made on europium(II) metaborate (EuB_2O_4) and Eu^{2+}-activated alkaline earth metaborates (SrB_2O_4:Eu^{2+} and CaB_2O_4:Eu^{2+}). The pressure–temperature phase diagram of EuB_2O_4 was determined by X-ray analysis. This diagram consists of the following four regions: phases I, III, and IV and the decomposed phase $EuB_4O_7 + Eu_2B_2O_5$. Phase EuB_2O_4 (IV) was paramagnetic whereas other phases were antiferromagnetic. It was found that the high-pressure phases of EuB_2O_4, SrB_2O_4:Eu^{2+}, and CaB_2O_4:Eu^{2+} gave the band emissions based on a $4f^7$–$4f^65d$ transition and the peak positions of their emissions shifted to long wavelength with transformation into the high-pressure phases. The emissions of EuB_2O_4 consist of a weak band at about 370 nm for the phases I and III, a band at about 410 nm for the phase IV, and two bands at about 368 and 395 nm for the decomposed phase. Also their emission intensities drastically increased with changing from phase III to IV; particularly SrB_2O_4(IV):Eu^{2+} was found to be an efficient photoluminescent material. Compound $Sr_{0.99}Eu_{0.01}B_2O_4$ gives a strong emission at 395 nm, and its quantum efficiency (about 60%) under an optimum (313 nm) excitation was about 100 times higher than that of the phase I. These results were discussed by considering the relationship between their crystal structures and theories for the magnetic interaction and energy transfer phenomena.

Introduction

Divalent europium, Eu(II), compounds have been synthesized because of their magnetic and spectroscopic properties. The arrangement of outer electrons of the Eu^{2+} ion is a $4f^7$ configuration, as well as the Gd^{3+} ion,[1] and some of Eu(II) compounds have unique magnetic properties on account of the magnetic exchange interactions between neighboring Eu^{2+} ions.[2-4] In addition the Eu^{2+} ion gives a line or a band emission based on the $4f^7$–$4f^7$ or the $4f^7$–$4f^65d$ transition,[5] and several Eu^{2+}-containing phosphates[6] and halides[7] are very efficient photoluminescent materials. Among Eu^{2+}-activated

*To whom correspondence should be addressed at the Department of Applied Chemistry, Faculty of Engineering.

(1) P. W. Selwood, *J. Am. Chem. Soc.*, **55**, 4869 (1933).
(2) (a) B. T. Matthias, R. M. Bozorth, and J. H. Van Vleck, *Phys. Rev. Lett.*, **7**, 1960 (1961); (b) T. R. McGuire, B. E. Argyle, M. W. Shafer, and J. S. Smart, *J. Appl. Phys.*, **34**, 1345 (1963); (c) T. R. McGuire and M. W. Shafer, *ibid.*, **35**, 984 (1964); (d) G. Fan and J. H. Greiner, *ibid.*, **41**, 1401 (1970); (e) J. C. Suits and K. Lee, *ibid.*, **42**, 3258 (1971); (f) G. Fan and R. A. Burn, *ibid.*, **42**, 3458 (1971).
(3) (a) T. R. McGuire, M. W. Shafer, R. J. Joenk, H. A. Alperin, and S. J. Pickart, *J. Appl. Phys.*, **37**, 981 (1966); (b) J. E. Greedan and G. J. McCarthy, *Mater. Res. Bull.*, **7**, 531 (1972).
(4) M. W. Shafer, T. R. McGuire, and J. C. Suits, *Phys. Rev. Lett.*, **11**, 251 (1963).

0020-1669/80/1319-0983$01.00/0

alkaline earth borates, only $BaB_8O_{13}:Eu^{2+}$ has been found to be an efficient phosphor.[8]

For metaborates M^IBO_2 and $M^{II}B_2O_4$, there are two types of chain construction, namely, one which consists of $(BO_2)_\infty$ chains sharing an oxygen of the BO_3 group (e.g., $LiBO_2$, CaB_2O_4, and SrB_2O_4)[9-11] and another which contains condensed-ring ions of three BO_3 units, $(B_3O_6)^{3-}$ (e.g., $NaBO_2$ and BaB_2O_4).[9,12,13] The borates of former type are easily transformed into several high-pressure phases, the triangularly coordinated borons in their units being partially or all changed into tetrahedrally coordinated borons by high-pressure treatments.[14-17]

The calcium metaborate CaB_2O_4 crystallizes with four different structures, three orthorhombic and one cubic modification. Phase CaB_2O_4 (I), which is stable at atmospheric pressure, contains only triangularly coordinated borons, and each Ca atom is surrounded by an 8-oxygen polyhedron. In CaB_2O_4 (II) 50% of the B atoms transform into the tetrahedral coordination, although the Ca atoms have the same coordination number, 8, as in CaB_2O_4 (I). Phase CaB_2O_4 (III) consists of a three-dimensional network of two triangular and four tetrahedral borons, a $(B_6O_{12})_\infty$ network, and 33% of the Ca atoms increase their coordination number from 8 to 10. Finally in CaB_2O_4 (IV) all B atoms are tetrahedrally coordinated, and this phase consists of a $(B_3O_6)_\infty$ network, and the coordination number of all B atoms increases to 12. On the other hand SrB_2O_4 can crystallize only with three forms different from the case of CaB_2O_4. Phase SrB_2O_4 (II) has not been obtained. Since the modifications of CaB_2O_4 and SrB_2O_4 are isostructural with each other, the boron and the strontium coordination numbers in each phase of SrB_2O_4 are the same values as those for the corresponding Ca analogues.

In the system $EuO-B_2O_3$ four europium(II) borates (viz., EuB_4O_7, EuB_2O_4, $Eu_2B_2O_5$, and $Eu_3B_2O_6$) have been obtained,[19] and $Eu_3B_2O_6$[19a] is a ferromagnet with the Curie point 7.5 K and EuB_2O_4[19b] antiferromagnetic below about 3 K. The tetraborate EuB_4O_7 gives a band emission based on the $4f^7-4f^65d$ transition of the Eu^{2+} ion.[19c]

The europium(II)-metaborate EuB_2O_4 also consists of $(BO_2)_\infty$ chains[19d] and is isostructural with phase I of CaB_2O_4 and SrB_2O_4, and it is expected that the similar polymorphism phenomenon to that of CaB_2O_4 and SrB_2O_4 will be observed on this borate. No work has been made on the luminescence properties of the high-pressure phases of Eu^{2+}-activated strontium and calcium metaborates. The present study has been carried out with a view to synthesize the high-pressure phases of EuB_2O_4, $SrB_2O_4:Eu^{2+}$, and $CaB_2O_4:Eu^{2+}$ and characterize them by X-ray analysis and magnetic susceptibility and ultraviolet luminescence measurements.

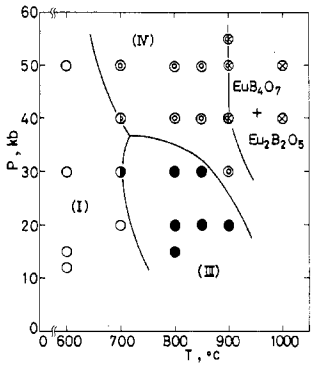

Figure 1. Phase diagram of EuB_2O_4: ○, I; ●, III; ◎, IV; ⊗, EuB_4O_7 + $Eu_2B_2O_5$.

Experimental Section

A. Preparation. The atmospheric pressure phase EuB_2O_4 (I) was prepared by heating a mixture of the appropriate amounts of Eu_2O_3 (99.99%), B (99.5%, reductant), and H_3BO_3 (99.5%) at 1000 °C for 3 h under vacuum according to the method described elsewhere.[19b] The Eu^{2+}-activated alkaline earth metaborates, $SrB_2O_4:Eu^{2+}$ and $CaB_2O_4:Eu^{2+}$, were obtained by following a standard ceramic technique: the appropriate amounts of H_3BO_3 and $SrCO_3:Eu^{3+}$ or $CaCO_3:Eu^{3+}$ coprecipitated from a dilute HCl solution of a reagent grade $Sr(NO_3)_2$ or $Ca(NO_3)_2$ and Eu_2O_3 by the slow addition of a $(NH_4)_2CO_3$ solution were fully mixed, pelletized, and heated at 1000 °C for 3 h in a reducing atmosphere of H_2.

The high-pressure treatments of the samples were carried out with a Dia 15 cubic anvil type apparatus in the following way: The powdered samples were packed into boron nitride cups, illustrated elsewhere.[20] After the samples were maintained at the desired high pressure and temperature conditions, the samples were quenched to room temperature, and then the pressure was released.

B. Characterization. X-ray powder analysis of resulting materials was performed with Ni-filtered Cu Kα radiation (λ = 1.5418 Å) monochromated by a graphite plate on a Rigaku Rota-flex diffractometer, which was calibrated with high-purity silicon (99.999%). The accurate lattice parameters of samples were determined by the least-squares method.

Magnetic susceptibility measurements were carried out with a Shimadzu MB-11 over a temperature range of 80–300 K.

Ultraviolet luminescence measurements of powder samples were made at room temperature with a Shimadzu recording absolute spectrofluorophotometer,[21] which can measure the corrected excitation and emission spectra by the automatic compensation and precalibration systems for the instrumental factors, and its slit widths were routinely set at 10 nm for excitation spectra and 5 nm for emission spectra. The quantum efficiencies of samples were measured by integrating the corresponding area below curves as "corrected emission spectra" under the excitation by a xenon lamp and with reference to a suitable standard phosphor, $CaWO_4:Pb^{2+}$ (NBS 1026). The quantum efficiency under 254-nm excitation at 300 K of the $CaWO_4:Pb^{2+}$ was defined as 76%.

Diffuse reflection spectra were measured with a Shimadzu multipurpose recording spectrophotometer equipped with an attachment for an integrating sphere. Magnesium oxide was used as the standard material, of which the reflection was defined as 100%.

Results

EuB_2O_4. The Eu(II) compounds are entirely isostructural with Sr analogues, since the radii of Eu^{2+} and Sr^{2+} ions are closely similar to each other; for example, an effective ionic radius in 8-coordination of O atoms is 1.25 Å for Eu^{2+} ion and

(5) G. Blasse, *Phys. Status Solidi B*, **55**, K131 (1973).
(6) C. C. Lagos, *J. Electrochem. Soc.*, **117**, 1189 (1970).
(7) (a) J. L. Sommerdijk, J. M. P. J. Verstegen, and A. Bril, *J. Lumin.*, **8**, 502 (1974); (b) A. L. N. Stevels and F. Pingault, *Philips Res. Rep.*, **30**, 277 (1975).
(8) G. Blasse, A. Bril, and J. de Vries, *J. Electrochem. Soc.*, **115**, 977 (1968).
(9) C. E. Weil and R. A. Schroeder, *J. Res. Natl. Bur. Stand., Sect. A*, **68**, 465 (1964).
(10) W. H. Zachariasen, *Acta Crystallogr.*, **17**, 749 (1964).
(11) M. Marezio, H. A. Plettinger, and W. H. Zachariasen, *Acta Crystallogr.*, **16**, 390 (1963).
(12) M. Marezio, H. A. Plettinger, and W. H. Zachariasen, *Acta Crystallogr.*, **16**, 594 (1963).
(13) A. D. Mighell, A. Perloff, and S. Block, *Acta Crystallogr.*, **20**, 819 (1966).
(14) C. H. Chang and J. L. Margrave, *Mater. Res. Bull.*, **2**, 929 (1967).
(15) M. Marezio and J. P. Remeika, *J. Chem. Phys.*, **44**, 3348 (1966).
(16) M. Marezio, J. P. Remeika, and P. D. Dernier, *Acta Crystallogr., Sect. B*, **25**, 955 (1969).
(17) M. Marezio, J. P. Remeika, and P. D. Dernier, *Acta Crystallogr., Sect. B*, **25**, 965 (1969).
(18) P. D. Dernier, *Acta Crystallogr., Sect. B*, **25**, 1001 (1969).
(19) (a) H. Hata, G. Adachi, and J. Shiokawa, *Mater. Res. Bull.*, **12**, 811 (1977); (b) K. Machida, H. Hata, K. Okuno, G. Adachi, and J. Shiokawa, *J. Inorg. Nucl. Chem.*, **41**, 1425 (1979); (c) K. Machida, G. Adachi, and J. Shiokawa, *J. Lumin.*, **21**, 101 (1979); (d) K. Machida, G. Adachi, and J. Shiokawa, *Acta Crystallogr., Sect. B*, **35**, 149 (1979).
(20) M. Shimada, N. Ogawa, M. Koizumi, F. Dachille, and R. Roy, *Am. Ceram. Soc., Bull.*, **58**, 519 (1979).
(21) T. Kurita, H. Yamamoto, M. Takada, and Y. Komurasaki, *Shimadzu Hyoron*, **32**, 225 (1975).

Table I. X-ray Diffraction Data for EuB_2O_4 (III)

hkl	d_{obsd}	d_{calcd}	I/I_0	*hkl*	d_{obsd}	d_{calcd}	I/I_0
200	6.23	6.22	10	610	1.972	1.973	45
002	5.77	5.71	15	520	1.966	1.968	40
110		5.71		602	1.953	1.949	25
011	5.70	5.60	25	611	1.944	1.944	45
201	5.48	5.46	30	521	1.938	1.939	40
111	5.13	5.11	20	423	1.919	1.928	45
210	4.67	4.47	20	315	1.909	1.910	35
202	4.20	4.21	50	232	1.907	1.910	50
211	4.17	4.16	25	330	1.901	1.904	60
112	4.06	4.04	50	006		1.903	
212	3.53	3.52	55	324	1.897	1.898	35
310	3.47	3.48	30	331	1.875	1.878	35
311	3.34	3.33	100	033	1.866	1.868	25
013	3.29	3.28	55	612	1.862	1.865	25
203	3.25	3.25	35	522	1.856	1.860	35
020	3.21	3.22	20	133	1.847	1.847	50
113	3.18	3.17	65	125	1.839	1.841	30
120	3.10	3.11	60	405		1.841	
400		3.11		603	1.819	1.821	20
121	3.00	3.00	90	206		1.820	
401		3.00		116	1.804	1.806	30
312	2.980	2.975	45	514	1.799	1.801	35
213	2.896	2.898	80	233	1.788	1.789	30
004	2.859	2.855	60	225	1.780	1.784	25
220	2.853	2.856	55	415	1.768	1.770	25
022	2.803	2.801	40	430	1.761	1.765	30
410		2.800		424	1.757	1.760	35
221	2.778	2.771	35	613	1.749	1.752	30
122	2.738	2.733	40	216		1.751	
402		2.731		523	1.746	1.748	20
411	2.722	2.719	35	431	1.741	1.744	20
204	2.596	2.595	45	621	1.721	1.722	25
313	2.571	2.570	35	710	1.710	1.713	25
114	2.560	2.554	40	333	1.699	1.703	20
222	2.554	2.554	45	134		1.698	
320	2.544	2.541	15	325	1.697	1.699	10
412	2.517	2.514	40	711	1.694	1.694	15
321	2.481	2.480	10	432	1.689	1.686	15
123	2.408	2.410	25	604	1.677	1.678	10
403		2.408		316	1.669	1.670	15
214	2.404	2.406	30	622	1.663	1.667	15
322	2.332	2.321	30	234	1.649	1.652	10
510		2.320		712	1.639	1.641	20
223	2.289	2.285	10	026	1.635	1.638	20
511	2.275	2.274	15	126	1.622	1.624	20
413	2.256	2.255	10	530		1.624	
420	2.241	2.235	10	614	1.620	1.624	20
314	2.216	2.208	15	406		1.623	
421	2.194	2.194	15	524	1.617	1.620	20
015	2.178	2.152	15	040	1.607	1.608	15
512	2.174	2.150	10	531		1.608	
205	2.146	2.144	35	433	1.599	1.601	15
024	2.138	2.135	20	425	1.596	1.598	10
115	2.120	2.121	35	140	1.591	1.594	10
323	2.114	2.113	25	226		1.584	
130	2.106	2.112	20	334	1.583	1.584	15
031	2.104	2.107	15	623		1.584	
124	2.102	2.104	25	017	1.579	1.581	10
404		2.103		141	1.577	1.579	15
422	2.079	2.081	15	207	1.575	1.578	10
131	2.073	2.077	15	416	1.573	1.574	25
600	2.069	2.073	20	117	1.567	1.569	15
601	2.038	2.040	20	035	1.562	1.563	20
215	2.031	2.034	15	532	1.559	1.562	20
230	2.020	2.026	30	713		1.562	
224	2.015	2.019	45	240	1.555	1.556	20
414	2.001	1.999	45	720	1.552	1.555	20
231	1.998	1.995	45	800		1.555	
132	1.982	1.981	40	135	1.549	1.551	20
514		1.981		042	1.544	1.547	20

1.26 Å for Sr^{2+} ion by Shannon.[22] Consequently the resulting phases of EuB_2O_4 from high-pressure treatments were identified by X-ray powder analysis on the basis of the lattice parameters of modifications of SrB_2O_4 and termed in a similar manner as the corresponding Ca and Sr analogues. The phase diagram of EuB_2O_4 is shown in Figure 1. This diagram consists of four regions: the first (atmospheric) phase EuB_2O_4 (I), the third phase EuB_2O_4 (III), the fourth phase EuB_2O_4 (IV), and the decomposed phase $EuB_4O_7 + Eu_2B_2O_5$. The second phase EuB_2O_4 (II) was not obtained as well as SrB_2O_4 (II). The X-ray patterns of EuB_2O_4 (III) and (IV) given in Tables I and II are very similar to those listed in the ASTM file.[23] Under the conditions above 40 kbar and 900 °C, EuB_2O_4 appeared to decompose into EuB_4O_7 and $Eu_2B_2O_5$ as follows:

$$3EuB_2O_4 \rightarrow EuB_4O_7 + Eu_2B_2O_5 \quad (1)$$

According to the above scheme, the overall mole number reduces from 3 to 2 and the volume of the sample also reduces to 87.5%. This agrees with the fact that one product of decomposition of SrB_2O_4 has been found to be SrB_4O_7 by Krogh-Moe.[24] The crystallinities of the resulting phases of EuB_2O_4 were generally low.

The accurate lattice parameters refined from the data listed in Tables I and II, the density, and the color of resulting phases of EuB_2O_4 are summarized in Table III. The phases EuB_2O_4 (III) and (IV) crystallize in the orthorhombic system C_{2v}^9-$Pna2_1$ with 12 molecules per unit cell and in the cubic system T_h^6-$Pa3$ with 12 molecules per unit cell, respectively. The observed density D_m of each phase is in good agreement with the calculated value D_x except EuB_2O_4 (IV): the values of D_m have been obtained on the sintered samples taken out from the boron nitride cell, and hence the pellet of EuB_2O_4 (IV) seems to contain some pores. The crystallographic properties of polymorphism of EuB_2O_4 are completely equal to those of SrB_2O_4, but the transition pressures and temperatures of both borates differ from each other: EuB_2O_4 (I) transforms into other phases at a higher temperature than that of SrB_2O_4 (I). This suggests that the bond strength of Eu–O must be stronger than that of Sr–O.

The magnetic and luminescence data of EuB_2O_4 given in Table IV are obtained for phase I (untreated), phase III (20

Table II. X-ray Diffraction Data for EuB_2O_4 (IV)

hkl	d_{obsd}	d_{calcd}	I/I_0	*hkl*	d_{obsd}	d_{calcd}	I/I_0
111	5.331	5.335	10	531	1.5629	1.5618	5
200	4.615	4.620	10	442, 600	1.5418	1.5400	10
210	4.137	4.132	30	610	1.5207	1.5190	5
211	3.776	3.772	35	532, 611	1.4996	1.4989	20
220	3.267	3.267	15	620	1.4617	1.4610	5
221	3.077	3.080	30	443, 621	1.4425	1.4430	5
311	2.787	2.786	100	504			
222	2.664	2.667	25	541	1.4262	1.4258	5
302	2.562	2.563	30	533	1.4090	1.4091	10
321	2.469	2.469	35	622	1.3925	1.3930	5
400	2.309	2.310	10	630, 542	1.3773	1.3774	10
322, 410	2.238	2.241	10	631	1.3628	1.3624	10
411	2.177	2.178	5	444	1.3346	1.3337	≃0
331	2.121	2.120	10	632	1.3219	1.3200	≃0
420	2.065	2.066	30	543	1.3062	1.3067	≃0
421	2.017	2.016	65	711, 551	1.2937	1.2939	≃0
332	1.9669	1.9700	25	640	1.2820	1.2814	≃0
422	1.8846	1.8861	20	702, 641	1.2691	1.2692	10
430	1.8455	1.8480	10	552, 633	1.2575	1.2574	10
431	1.8139	1.8121	5	721			
333, 511	1.7777	1.7782	35	642	1.2344	1.2347	5
432, 502	1.7151	1.7158	15	544, 722	1.2237	1.2239	0
521	1.6862	1.6870	20	731, 553	1.2033	1.2029	15
440	1.6327	1.6334	20	643, 650	1.1824	1.1831	5
441	1.6086	1.6085	5	732, 651	1.1735	1.1735	5
433	1.5807	1.5846	5	800	1.1550	1.1550	5

(22) R. D. Shannon, *Acta Crystallogr., Sect. A*, **32**, 225 (1975).

(23) The file of X-ray powder diffraction standards by the American Society for Testing and Materials. Inorganic compounds: SrB_2O_4 (III), 22-1418; SrB_2O_4 (IV), 22-1419.

(24) J. Krogh-Moe, *Acta Chem. Scand.*, **18**, 2055 (1964).

Table III. High-Pressure Polymorphism of EuB_2O_4

phase	lattice parameters, Å: CaB_2O_4[a]	lattice parameters, Å: SrB_2O_4[a]	lattice parameters, Å: EuB_2O_4	space group	Z	density, g cm^{-3}: D_m	density, g cm^{-3}: D_x	color
I	a = 6.214 b = 11.604 c = 4.284	a = 6.589 b = 12.018 c = 4.337	a = 6.593 (1) b = 12.063 (2) c = 4.343 (1)	D_{2h}^{14}-*Pnca*	4	4.61[b]	4.57	light yellow
12 kbar ↓								
II	a = 8.369 b = 13.816 c = 5.007	8 kbar ↓		D_{2h}^{10}-*Pccn*	8			
15 kbar ↓								
III	a = 11.380 b = 6.382 c = 11.304	a = 12.426 b = 6.418 c = 11.412	a = 12.44 (1) b = 6.43 (1) c = 11.42 (1)	C_{2v}^{9}-*Pna*2$_1$	12	5.22[c]	5.18	yellow
25 kbar ↓		15 kbar ↓						
IV	a = 9.008	a = 9.222	a = 9.240 (1)	T_h^6-*Pa*3	12	5.57[c]	6.00	yellow
EuB_4O_7 + $Eu_2B_2O_5$						5.40[c]	5.22	dark yellow

[a] Reference 18. Treatment temperature = 600 °C for SrB_2O_4 and 900 °C for CaB_2O_4. [b] Reference 19d. [c] Data were obtained on the sintered samples with the dimension: ca. 4 mm × 3 mm.

Table IV. Magnetic and Luminescence Data for the Various Phases of EuB_2O_4

	phase	treatment: P, kbar	treatment: T, °C	μ_{eff}, μ_B[a]	Θ_c, K[b]	λ_{max}, nm[c]	I[d]
a	I			7.88	−5	370	very weak
b	III	20	800	7.42	−5	370	very weak
c	IV	50	850	7.62	0	410	weak
d	EUB_4O_7 + $Eu_2B_2O_5$	50	1000	7.54	−10	368, 395	weak

[a] μ_{eff} = magnetic moment per Eu^{2+} ion. The theoretical value is 7.94 μ_B. [b] Θ_c = paramagnetic Curie temperature. The measured range is 80–300 K. [c] λ_{max} = position of the maximum of emission band at 300 K. [d] I = emission intensity.

kbar, 800 °C), phase IV (50 kbar, 850 °C), and the decomposed phase (50 kbar, 1000 °C). Since the effective magnetic moment per Eu^{2+} ion (μ_{eff}) of EuB_2O_4 (I) is in good agreement with the theoretical value 7.94 μ_B, the Eu atoms exist in divalent state. However, the values of other phases are slightly smaller than the theoretical one. This implies that a very small amount of Eu^{2+} ion has been oxidized into Eu^{3+} ions in the high-pressure treatments because a μ_{eff} value of the Eu^{3+} ion is about 3.6 μ_B.[25] The paramagnetic Curie temperature Θ_c was about −5 K for phase III, about 0 K for phase IV, and about −10 K for the decomposed phase, respectively. The magnetic properties of compounds can be approximately discussed on the basis of the sign of the Θ_c value. In general the Θ_c value is minus for antiferromagnets and plus for ferromagnets, and hence paramagnets should have a value of zero. The phase EuB_2O_4 (I) has been found to be an antiferromagnet with T_N = 3 K and Θ_c = −5 K. (The value reported in ref 19b, Θ_c = −10 K, has been erroneously treated in the least-squares process. Consequently the value listed in this journal, Θ_c = −5 K, is more accurate.) It can be therefore presumed from the Θ_c values that phase III and decomposed phase are antiferromagnetic, and phase IV is paramagnetic at low temperature.

The high-pressure phases of EuB_2O_4 were found to give the band emission based on the $4f^7$–$4f^65d$ transition of the Eu^{2+} ion, and the peak positions of their emissions shift to long wavelength and their light outputs slightly increased with transformation into phase IV and the decomposed phase. The emission spectral distribution and the excitation spectra of phase IV and the decomposed phase are shown in Figure 2. The emission intensity for any modification of EuB_2O_4 was weak. Their emission patterns were illustrated on the basis of the energy output of the photomultiplier. The emission of phase IV and the decomposed phase consists of a band at about

(25) D. J. Craik, "Magnetic Oxides Part I", Wiley, New York, 1975, p 12.

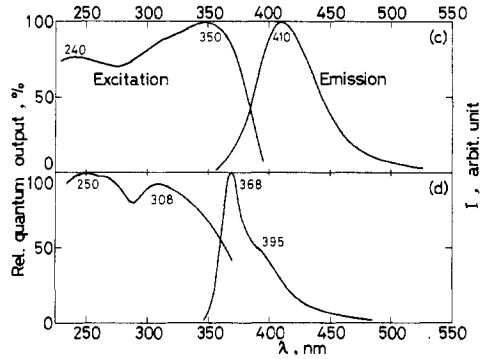

Figure 2. Spectral energy distribution and relative excitation spectra of the emissions of EuB_2O_4 (III) and (IV).

Table V. Resulting Phase and Luminescence Data of $Sr_{0.99}Eu_{0.01}B_2O_4$ from High-Pressure Treatments

	phase	P, kbar[a]	λ_{max}, nm	QE, %[b]
a	I		367	1
b	III	15	367	1
c	IV + III (minor)	20	404	30
d	IV	30	395	39

[a] Treatment temperature = 700 °C. [b] QE = quantum efficiency under 254 nm excitation at 300 K.

410 nm and two bands at about 368 and 395 nm, respectively, although phases I and III give a very weak emission at about 370 nm. The emission at about 370 nm of the decomposed phase must be attributed to one product of decomposition, EuB_4O_7, since it gives a relatively strong emission at about 370 nm.[19c]

SrB_2O_4:Eu^{2+} and CaB_2O_4:Eu^{2+}. For the luminescence properties of Eu^{2+} ion in high-pressure phases of metaborate, the high-pressure treatments and luminescence measurements were made on Eu^{2+}-activated alkaline earth metaborates, SrB_2O_4:Eu^{2+} and CaB_2O_4:Eu^{2+}. The resulting phases of $Sr_{0.99}Eu_{0.01}B_2O_4$ from the treatments at 15–30 kbar and 700 °C and their luminescence data are shown in Table V and Figure 3. It is seen that the emission peak positions of samples containing the phase IV shift to long wavelength and their bandwidths at half maximum increase from 20 to 43 nm compared with those of other phases. Whereas the peak positions of phases I and III are 367 nm and their emission shapes are closely similar to each other, phase IV gives a strong emission peaking at 395 nm. Sample c of phase IV mixed with a small amount of phase III gives an emission at 404 nm, which is positioned at a slightly longer wavelength than that of the pure phase of $Sr_{0.99}Eu_{0.01}B_2O_4$ (IV). All phases of SrB_2O_4:Eu^{2+} give the excitation spectra consisting of two bands

Table VI. Resulting Phase and Luminescence Data[a] of $Ca_{1-x}Eu_xB_2O_4$ from High-Pressure Treatments

treatment[b]		phase and luminescence data				
P, kbar	*T*, °C	CaB_2O_4	$Ca_{0.99}Eu_{0.01}B_2O_4$	$Ca_{0.97}Eu_{0.03}B_2O_4$	$Ca_{0.94}Eu_{0.06}B_2O_4$	$Ca_{0.90}Eu_{0.10}B_2O_4$
		I	I; about 450 nm; very weak	I; about 450 nm; weak	I; 368, 477 nm; <1%	I; 367, 479 nm; <<1%
13	900	I, II	(b) I, II; 363 nm; weak		I; 367, 458 nm; 2%	
15	800			II, III; 363 nm; <1%		
15	900				I; 366 nm; 2%	
18	900			III; 363 nm; <1%	(c) III; 364 nm; 3%	
20	800			III; 360, 395 nm; <1%		
20	900	III	III; 362 nm; weak	III, IV; 361, 396 nm; 2%	(d) III; 364, 399 nm; 5%	
22	900				IV, III; 362, 395 nm; 9%	
30	900	IV	IV; 359 nm; 26%		(e) IV; 362, 394 nm; 32%	
31	900			IV; 361, 395 nm; 18%	IV; 361, 394 nm; 13%	

[a] The values of λ_{max} and QE under 254-nm excitation at 300 K are listed in this table. [b] Treatment period = 30-60 min.

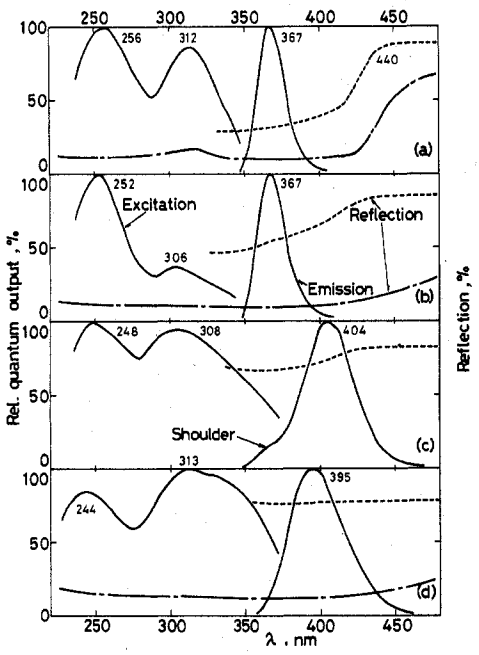

Figure 3. Relative emission and excitation spectra (solid line) for the various phases of $Sr_{0.99}Eu_{0.01}B_2O_4$ and diffuse reflection spectra (dashed line for $Sr_{0.99}Eu_{0.01}B_2O_4$ and dashed-dotted line for EuB_2O_4).

peaking at 250 ± 6 and 310 ± 4 nm. The fivefold degenerated d level of the excited ($4f^65d$) configuration is split into several levels by the crystal field formed by anions around the Eu^{2+} ions. In solids the absorption of Eu^{2+} ions in the near-ultraviolet region is generally agreed to be attributable to the 4f → 5d transition,[26] and the matrix SrB_2O_4 has no absorption band in this region. Therefore the excitation patterns mentioned above should be due to the splitting of the 5d level.

It was found that the quantum efficiency of samples remarkably increased with transformation into phase IV. The treatment pressure dependence of the quantum efficiency of $Sr_{0.99}Eu_{0.01}B_2O_4$ is shown in Figure 4. It is noticeable that the quantum efficiency drastically increases to about 50 times under 254-nm excitation and about 100 times under an optimum (313 nm) excitation for phase IV with transformation from phase III to IV. In Figure 5 we summarize the Eu^{2+} concentration quenching effect to the quantum efficiency of $Sr_{1-x}Eu_xB_2O_4$ (IV). An optimum concentration is seen to be about 1 atom %, at which its quantum efficiency is about 40% under 254-nm excitation and about 60% under 313-nm excitation. Since this value is as high as that of $BaB_8O_{13}:Eu^{2+}$ which is an efficient phosphor, SrB_2O_4 (IV):Eu^{2+} is also an efficient one.

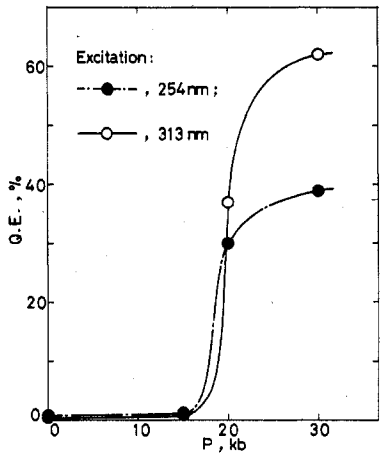

Figure 4. Quantum efficiency vs. treatment pressure for $Sr_{0.99}Eu_{0.01}B_2O_4$.

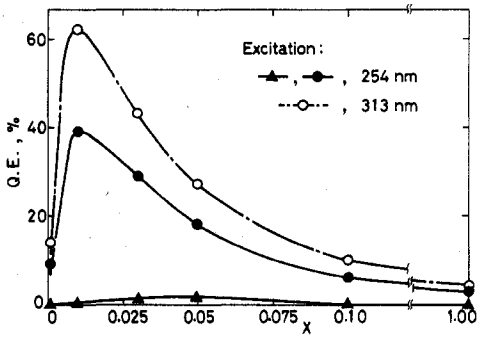

Figure 5. Quantum efficiency vs. Eu^{2+} content, *x*, for the phases of $Sr_{1-x}Eu_xBu_2O_4$: ▲, I; ● and ○, IV.

The resulting phases of $CaB_2O_4:Eu^{2+}$ from the treatments at the various conditions and their luminescence data are summarized in Table VI and Figure 6. The borate CaB_2O_4 crystallizes with four different structures. However no pure phase of CaB_2O_4 (II):Eu^{2+} was obtainable. The fact that phase II hardly forms with increasing the value of *x* in $Ca_{1-x}Eu_xB_2O_4$ is due to a crystallographic mismatching between the radii of Ca^{2+} and Eu^{2+} ions. The luminescence properties of the modifications of $CaB_2O_4:Eu^{2+}$ considerably differ from those of $SrB_2O_4:Eu^{2+}$. Phase I of $Ca_{0.94}Eu_{0.06}B_2O_4$ gives two emission bands peaking at 368 and 477 nm; its excitation spectra consist of a broad band at 321 nm for the 477-nm emission band and two bands at 255 and 316 nm for the 368-nm emission band. For the mixed phase of $Ca_{0.99}Eu_{0.01}B_2O_4$ (I) and (II) the emission spectrum consists of a band at about 363 nm, and its excitation pattern has two peaks at about 250 and 300 nm as well as that of the 368-nm emission band of phase I. Phase $Ca_{0.94}Eu_{0.06}B_2O_4$ (III) was found to give two types of emission

(26) D. S. McClure and Z. J. Kiss, *J. Chem. Phys.*, **39**, 3251 (1963).

Table VII. Lattice parameters[a] for CaB_2O_4 and $Ca_{0.94}Eu_{0.06}B_2O_4$ (I–IV), Å

compd	I	II	III	IV
CaB_2O_4	$a = 6.215$ (3)	$a = 8.38$ (7)	$a = 11.378$ (2)	$a = 9.021$ (6)
	$b = 11.611$ (4)	$b = 12.72$ (6)	$b = 6.3825$ (7)	
	$c = 4.280$ (2)	$c = 4.94$ (7)	$c = 11.310$ (1)	
$Ca_{0.94}Eu_{0.06}B_2O_4$	$a = 6.259$ (5)		$a = 11.403$ (2)	$a = 9.0196$ (6)
	$b = 11.623$ (6)		$b = 6.390$ (7)	
	$c = 4.282$ (3)		$c = 11.307$ (4)	

[a] Refinement range = $0.11 < (\sin\theta/\lambda) < 0.32$ Å^{-1}.

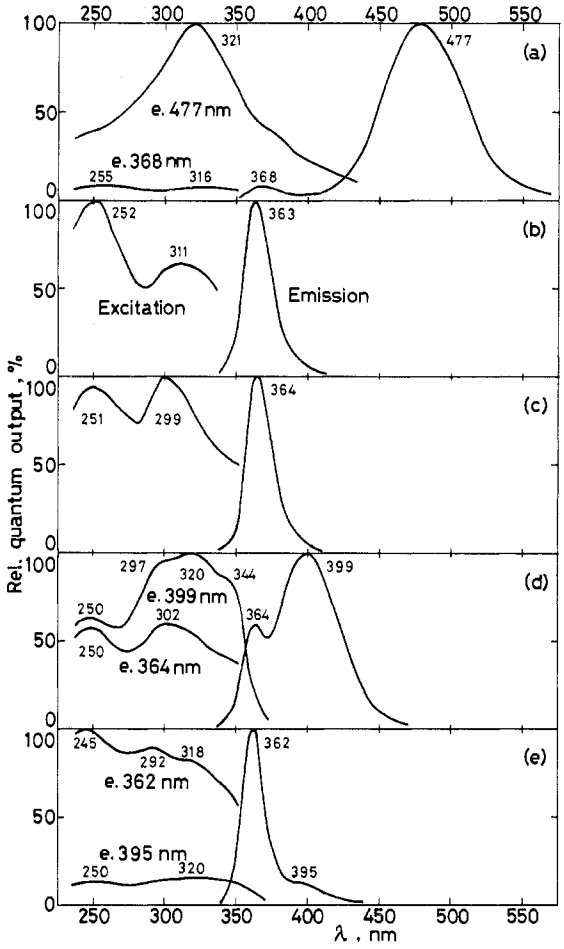

Figure 6. Relative emission and excitation spectra for the various phases of $Ca_{0.94}Eu_{0.06}B_2O_4$ ($Ca_{0.99}Eu_{0.01}B_2O_4$ for (b)).

patterns depending on the treatment conditions. One type was observed on sample c treated at 18 kbar and 900 °C. Its emission and excitation spectra consist of a band and two bands similar to the patterns observed on the mixed-phase sample b, respectively. Another type, viz., sample d obtained at the treatment condition of 20 kbar and 900 °C, gives two emission bands peaking at 364 and 399 nm, and its excitation spectra consist of four bands at about 250, 297, 320, and 344 nm for the 399-nm emission band and two bands at about 250 and 302 nm for the 364-nm emission band. These excitation patterns differ from each other; particularly the excitation spectrum of the 399-nm emission band is specific among a series of high-pressure phases of CaB_2O_4:Eu^{2+}. The emission pattern of $Ca_{0.94}Eu_{0.06}B_2O_4$ (IV) is peaking at 362 and 395 nm, and its excitation spectra have three peaks at 245, 292, and 318 nm for the 362-nm emission band. The quantum efficiencies of CaB_2O_4:Eu^{2+} are also observed to increase with transformation into the higher pressure phase. It is noticeable that the emission bands around 365 nm of samples a, b, c, and d are similar to those of phases I and III of EuB_2O_4 and SrB_2O_4:Eu^{2+}, the band at 399 nm of sample d to that of EuB_2O_4 (IV) and SrB_2O_4 (IV):Eu^{2+}, and the pattern of sample e to that of the decomposed phase of EuB_2O_4, respectively.

In order to interpret these phenomena, we measured the lattice parameters of the resulting phases of $Ca_{0.94}Eu_{0.06}B_2O_4$ over a range $0.11 < (\sin\theta/\lambda) < 0.32$ Å^{-1}. In Table VII their lattice parameters are summarized together with those of CaB_2O_4 measured at the same condition. The lattice parameters of CaB_2O_4 are larger than those of EuB_2O_4 because of the difference between the radii of Ca^{2+} and Eu^{2+} ions. For phase I, the lattice parameters of $Ca_{0.94}Eu_{0.06}B_2O_4$ should be larger than those of CaB_2O_4, but those of the other phases of CaB_2O_4 and $Ca_{0.94}Eu_{0.06}B_2O_4$ are very close to each other. This suggests that the EuB_2O_4 phase is pressed out from the CaB_2O_4:Eu^{2+} phase by the high-pressure treatments, and hence the emission patterns of CaB_2O_4:Eu^{2+} are assigned as follows: for phase I the emission at about 477 nm corresponds to the band from the Eu^{2+} ions in the matrix CaB_2O_4 (I) because the emission at 368 nm must be derived from EuB_2O_4 (I) in the grain boundaries. The fact that the emission peak position of CaB_2O_4 (I):Eu^{2+} (477 nm) considerably shifts to long wavelength compared with those of SrB_2O_4 (I):Eu^{2+} and EuB_2O_4 (I) may be due to a strain of the matrix induced by substituting the larger Eu^{2+} ions for the smaller Ca^{2+} ions. On the basis of the phase diagram of EuB_2O_4 (see Figure 1) the emissions at about 364 nm of sample b, c, and d are identified with the EuB_2O_4 (III) phase and the band at 399 nm of sample d corresponds to the emission pattern of EuB_2O_4 (IV), although the peak positions of the corresponding emissions from EuB_2O_4 and CaB_2O_4:Eu^{2+} somewhat deviate from each other. The emission pattern of sample e results from the decomposed phase of EuB_2O_4 in the grain boundaries of CaB_2O_4 (IV). Consequently it is concluded that the luminescence properties of the high-pressure phases of CaB_2O_4:Eu^{2+} are due to those of the EuB_2O_4 phase pressed out from the matrix CaB_2O_4. The fact that the quantum efficiencies of the high-pressure phases of CaB_2O_4:Eu^{2+} are relatively greater than those of EuB_2O_4 may be attributable to the decrease of the concentration quenching effect by dispersing the EuB_2O_4 phase into the grain boundaries of CaB_2O_4.

Discussion

Among the modifications of CaB_2O_4 and SrB_2O_4 the detailed structure analysis has been performed only on the phases CaB_2O_4(I),[11] (III)[16] and (IV),[17] and EuB_2O_4 (I) has been found to be entirely isostructural with CaB_2O_4 (I).[19d] The structures of EuB_2O_4 (I) and CaB_2O_4 (III) and (IV) are illustrated in Figure 7. In EuB_2O_4 (I) each Eu atom occupies a 4*c* site of space group D_{2h}^{14}-*Pnca* and is surrounded by 8 oxygens. On the assumption that all atoms in the high-pressure phases of EuB_2O_4 are coordinated in a similar manner as those of CaB_2O_4, EuB_2O_4 (III) has three kinds of sites, Eu(1), Eu(2), and Eu(3), which belong to a 4*a* site of space group C_{2v}^{9}-*Pna*2_1, and the coordination numbers of oxygen around the Eu atoms on those sites are 8 for Eu(1) and Eu(2) and 10 for Eu(3), respectively. While in EuB_2O_4 (IV) Eu atoms are placed on two sites, Eu(1) and Eu(2), which belong to 4*a* and 8*c* sites of space group T_h^6-*Pa*3 and those sites are surrounded by 12 oxygens. Phases I, III, and IV consist of $(BO_2)_\infty$ chains, a network of B_6O_{12} units with two triangular and four tetrahedral

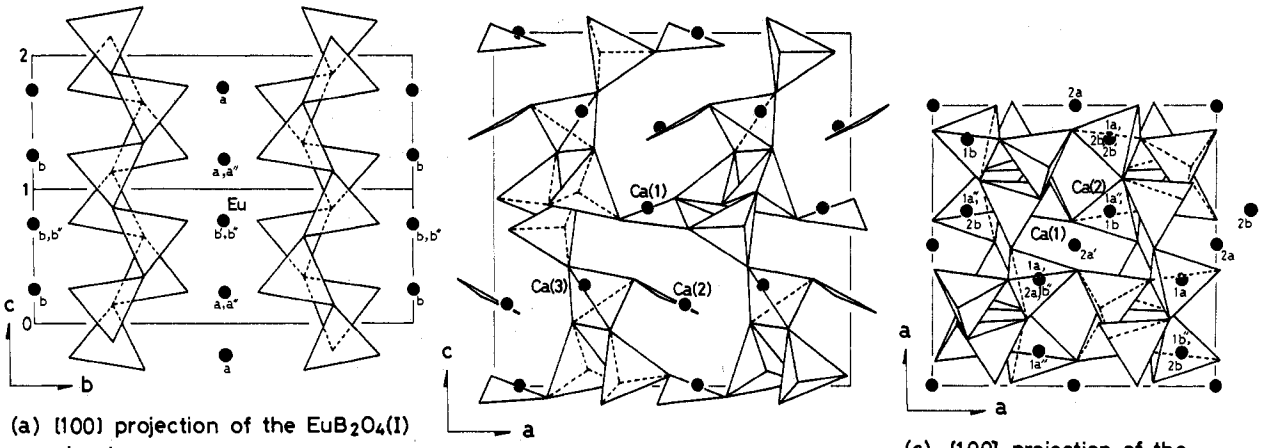

(a) [100] projection of the EuB_2O_4(I) structure.

(b) [010] projection of the CaB_2O_4(III) structure.

(c) [100] projection of the CaB_2O_4(IV) structure.

Figure 7. Structures for the high-pressure phases of $M^{II}B_2O_4$: (a) nearest neighboring Eu atoms; (b) next-nearest neighboring Eu atoms. Superscripts (′) and (″) represent the Eu atoms in the upper and the lower cell, respectively.

Table VIII. Interatomic Distances in EuB_2O_4 (I) and (IV), Å

phase	Eu–O	Eu–Eu: nearest neighbors	Eu–Eu: next-nearest neighbors
I[a]	2.624 (×8)	4.080 (×6)	6.632 (×10)
IV[b]	Eu(1) 2.80 (×12)	3.83 (×6)	6.00 (×4)
	Eu(2) 2.97 (×12)	3.89 (×4)	5.15 (×5)

[a] Reference 19d. [b] The values were estimated on the basis of atomic parameters of CaB_2O_4.

borons, and a network of B_3O_6 units with three tetrahedral borons, respectively. It is noticeable that each Eu^{2+} ion in EuB_2O_4 (IV) is considerably isolated from the neighboring Eu^{2+} ions by the surrounding BO_4 units compared with the cases of EuB_2O_4 (I) and (III).

The magnetic properties of Eu(II) compounds are approximately understood by considering the magnitude of the magnetic exchange and superexchange via O^{2-} ion interactions between the neighboring Eu^{2+} ions. In the case of europium(II) chalcogenides[2b,c] and titanates,[3] their magnetisms are mainly attributable to ferromagnetic Eu^{2+}–Eu^{2+} exchange and antiferromagnetic 90° Eu^{2+}–O^{2-}–Eu^{2+} superexchange interactions between the nearest neighboring Eu^{2+} ions and a 180° Eu^{2+}–O^{2-}–Eu^{2+} superexchange interaction (ferromagnetic or, as the case may be, antiferromagnetic) between the next-nearest neighboring Eu^{2+} ions, respectively. These interactions are sensitive to the interatomic Eu^{2+} spacings since the interactions between Eu^{2+} ions have been regarded as taking place via an overlap of 4f–5d orbitals.[27,28] The interatomic distances between the neighboring Eu and O atoms in EuB_2O_4 (I) and (IV) are given in Table VIII. The crystal structure of EuB_2O_4 (III) was too complex to discuss its magnetism.

The mean distance between the nearest neighboring Eu^{2+} ions is 4.080 Å for EuB_2O_4 (I) and 3.83 Å for the Eu(1) site and 3.89 Å for the Eu(2) site in EuB_2O_4 (IV). The fact that EuB_2O_4 (I) is an antiferromagnet with T_N = 3 K is due to the fact that the magnetic interaction between the nearest neighboring Eu^{2+} ions located in the (010) and (020) planes is expected to contribute to the ordering of spins only in those planes.[19b,d] The mean distance between the next-nearest neighboring Eu^{2+} ions around the Eu(2) site in EuB_2O_4 (IV) is 5.15 Å and effective for the 180° Eu^{2+}–O^{2-}–Eu^{2+} interaction,

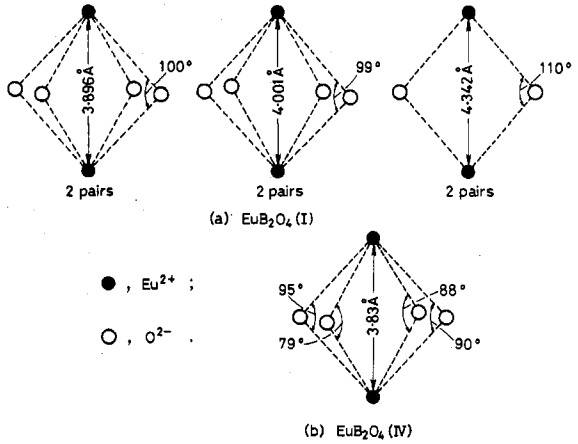

Figure 8. Anion environment around nearest-neighboring Eu^{2+} ions in EuB_2O_4 (I) and (IV).

but other distances longer than that are enough to interact with neighboring Eu^{2+} ions on the basis of other Eu(II) compounds.[3b] Consequently we consider here the magnetism of EuB_2O_4 (IV) on the basis of the magnetic interactions between the nearest neighboring Eu^{2+} ions and between the next-nearest neighboring Eu^{2+} ions around the Eu(2) site. The anion environments around the nearest neighboring Eu^{2+} pairs in EuB_2O_4 (I) and (IV) are shown in Figure 8.

For EuB_2O_4 (I), there are two types of interaction among the six nearest neighboring Eu^{2+} pairs: the first type is closely similar to that found in $EuTiO_3$[3a] which is an antiferromagnet with T_N = 5.3 K. In EuB_2O_4 (I), four 90° Eu^{2+}–O^{2-}–Eu^{2+} superexchange interactions are dominant although the Eu^{2+}–O^{2-}–Eu^{2+} angles (99 and 100°) somewhat deviate from the value of 90°, since the Eu^{2+}–Eu^{2+} interaction is weak because the distance between the nearest neighboring Eu^{2+} pairs (3.896 and 4.001 Å) is not enough for its interaction. Therefore the contribution of this type to the magnetism is antiferromagnetic. However both of the exchange and superexchange interactions for the second type are weak because of the long distance between the nearest neighboring Eu^{2+} pair (4.342 Å) and the large deviation of the Eu^{2+}–O^{2-}–Eu^{2+} angle (110°) from the value of 90°. Therefore EuB_2O_4 (I) is antiferromagnetic at low temperature owing to the contribution of the superexchange interaction of the first type.

On the other hand the anion environments around the nearest neighboring Eu^{2+} ions in EuB_2O_4 (IV) are mainly the same type as the first one of EuB_2O_4 (I) and a nearest

(27) J. B. Goodenough, "Magnetism and the Chemical Bond", Interscience, New York, 1963, p 146.
(28) T. Kasuya, *IBM J. Res. Dev.*, **14**, 214 (1970).
(29) D. L. Dexter, *J. Chem. Phys.*, **21**, 836 (1953).

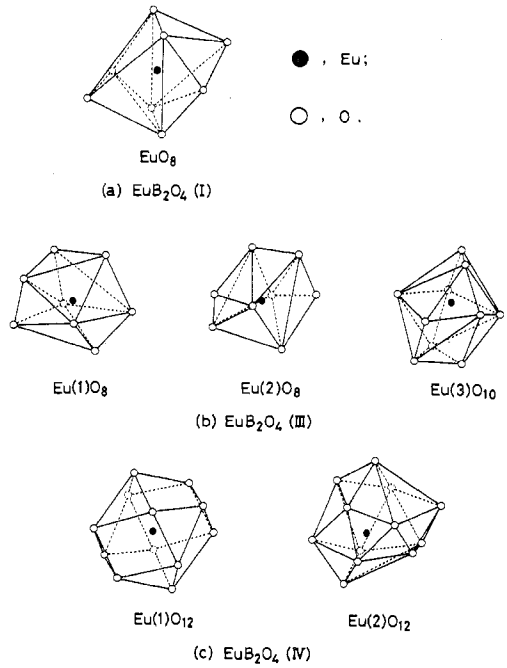

Figure 9. Oxygen coordination around Eu atoms in the high-pressure phases of EuB_2O_4.

neighboring Eu^{2+} pair has four 90° Eu^{2+}–O^{2-}–Eu^{2+} superexchange pairs. The Eu^{2+}–Eu^{2+} distance is shorter than that of the first type of EuB_2O_4 (I), and hence the Eu^{2+}–Eu^{2+} interaction in EuB_2O_4 (IV) is not weaker than that in EuB_2O_4 (I). If the contribution of the ferromagnetic Eu^{2+}–Eu^{2+} interaction to the magnetism is equal to that of the antiferromagnetic 90° Eu^{2+}–O^{2-}–Eu^{2+} interaction, the overall contribution of the magnetic interactions between the nearest neighboring Eu^{2+} ions should be paramagnetic. The 180° Eu^{2+}–O^{2-}–Eu^{2+} interaction between the next-nearest neighboring Eu^{2+} ions seems to be effective on the basis of the Eu^{2+}–Eu^{2+} distance and the Eu^{2+}–O^{2-}–Eu^{2+} angle: the Eu^{2+}–Eu^{2+} distance is 5.15 Å and enough to interact with the neighboring Eu^{2+} ions although the Eu^{2+}–O^{2-}–Eu^{2+} angle (162°) deviates from the value of 180°. However, all of the next-nearest neighboring Eu^{2+} ions which take part in this interaction are only those occupying the Eu(2) site and cannot interact with the neighboring Eu^{2+} ions on the Eu(1) site (see Figure 7), and hence the contribution of the overall magnetism of EuB_2O_4 (IV) must be small. Therefore the magnetic behavior of EuB_2O_4 (IV) is expected to be paramagnetic. However, the fact that the decomposed phase EuB_4O_7 + $Eu_2B_2O_5$ had the tendency to be antiferromagnetic although EuB_4O_7 and $Eu_2B_2O_5$ were paramagnetic[19b] could not be elucidated.

The emissions based on the $4f^7$–$4f^65d$ transition strongly depend on anions and their arrangement around Eu^{2+} ions because of the broadly spaced d orbital, whereas the $4f^7$–$4f^7$ line emission is scarcely affected with the crystal field.[5] The EuO_n polyhedra formed by oxygens around Eu^{2+} ions in the high-pressure phases are schematically illustrated in Figure 9. The symmetries of their polyhedra are very low except for the $Eu(1)O_{12}$ polyhedron in phase IV which is cubically close packed. For phases I and III, the symmetries of EuO_8 and EuO_{10} polyhedra are seen to be relatively similar to each other, but phase IV has the EuO_{12} polyhedra with a different symmetry from that of other phases. The assignment of their excitation spectra was unsuccessful because it was difficult to estimate the split energy levels of the 5d orbital of Eu^{2+} ions by the crystal field.

The emission peak positions of the high-pressure phases can be qualitatively interpreted by considering their emission processes on the basis of a configurational-coordinated diagram.[5] The absorption corresponds to the transition $4f \rightarrow 5d$, and then the electrons in the excited ($4f^65d$) state move to the equilibrium distance (r_e) and undergo transition to the ground ($^8S_{7/2}$) state. In this process, the value of r_e is not necessarily equal to that of the ground state (r_0) since the $4f^65d$ level strongly depends on the crystal field around the Eu^{2+} ion. For SrB_2O_4 (I):Eu^{2+} or SrB_2O_4 (III):Eu^{2+}, the electrons which are excited by absorbing the energy of 4–5 eV (250–310 nm) transfer to the ground state at the equilibrium distance (r_e^{I} or r_e^{III}), whereupon the emission at 367 nm is to be observed. If the minimum of the $4f^65d$ level of phase IV is slightly lowered or shifted to the right (Stokes shift: $\Delta r_e^{IV} < \Delta r_e^{I}$ or Δr_e^{III}) compared with that of phase I or III owing to the effect of its above-mentioned crystal field, the emission peak position of phase IV should shift to long wavelength. A nonradiative process from the excited to the ground state requires an activation energy ΔE, and if this value is very great, the possibility of the nonradiative process is very small. However the difference between the activation energy, ΔE^{I} or ΔE^{III} for phase I or III and ΔE^{IV} for phase IV, is expected to be very small, and this cannot account for the fact that the quantum efficiency drastically increases with transformation into phase IV.

For the purpose of interpretation of this phenomenon, we measured reflection spectra on the high-pressure phases of $Sr_{0.99}Eu_{0.01}B_2O_4$ and EuB_2O_4 (see Figure 3). However, we could not obtain their reflection patterns at a shorter wavelength than their emission peak positions, since the measured reflection spectra were mixed with the emissions from the samples owing to the integrating sphere attachment of the spectrophotometer, except those of the EuB_2O_4 modifications of which the emissions are very weak. For $Sr_{0.99}Eu_{0.01}B_2O_4$, phase I gives a broad band with the absorption edge at about 440 nm, and the emission band is completely included in this absorption region. The absorption edge shifts to short wavelength with transformation into the higher-pressure phase, and sample d (the pure phase of IV) no longer gives an apparent absorption edge. Phases EuB_2O_4 (I), (III), and (IV) give broad absorption bands, which completely include the corresponding emission bands. This suggests that some 5d levels of Eu^{2+} ions in the modifications of EuB_2O_4 are lowered by the interaction between the neighboring Eu^{2+} ions compared with the luminescent center, and the absorption in those levels cannot contribute to emit. The fact that the absorption spectra of EuB_2O_4 (III) and (IV) are not sharp compared with that of EuB_2O_4 (I) must be due to their low crystallinity. It is noticeable that the absorption spectra of EuB_2O_4 (I) and $Sr_{0.99}Eu_{0.01}B_2O_4$ (I) are closely similar to each other, and their emission bands completely overlap the absorption spectra. In general the reflection spectra of Eu^{2+}-activated phosphors correspond to their excitation patterns except for the absorption of matrixes, and the degree of the emission and reflection spectra is relatively small. That is in good agreement with the case of $Sr_{0.99}Eu_{0.01}B_2O_4$ (IV) but not with the case of $Sr_{0.99}Eu_{0.01}B_2O_4$ (I) and (III). If the Eu^{2+} ions in SrB_2O_4:Eu^{2+} form a kind of "cluster", namely, a number of Eu^{2+} ions localized in a region of which the Eu^{2+} concentration is very high and enough to interact with the neighboring Eu^{2+} ions, SrB_2O_4:Eu^{2+} gives the same absorption pattern as EuB_2O_4.

From Figure 7, phases I, III, and IV consist of $(BO_2)_\infty$ chains, the $(B_6O_{12})_\infty$ network, and the $(B_3O_6)_\infty$ network, respectively, and the lower pressure phase is seen to be the more "open" structure than the higher pressure one. It seems that the sites which the Eu^{2+} ions in SrB_2O_4 (I):Eu^{2+} can occupy are located on (010) and (020) planes, and the Eu^{2+} ions have a tendency to be concentrated on those planes. However, such tendency in SrB_2O_4 (IV):Eu^{2+} must be very small since the

Eu^{2+} ions are completely surrounded by the BO_4 units of the $(B_3O_6)_\infty$ network and hardly migrate to other sites. Consequently the amount of the cluster in SrB_2O_4 (IV):Eu^{2+} must be smaller than that of other phases. This is supported by the following facts: (a) the reflection patterns of phase I or III of SrB_2O_4:Eu^{2+} and EuB_2O_4 are in agreement with each other different from those of phase IV. (b) SrB_2O_4 (I):Eu^{2+} in which the Eu^{2+} concentration is relatively high (>10 atom %) has a tendency to be $\Theta_c < 0$ K, and this suggests magnetic interactions between the neighboring Eu^{2+} ions. (c) The color of SrB_2O_4 (I):Eu^{2+} changes from pale yellow-white to white with transformation into the high-pressure phases because the cluster should be colored with light yellow as well as EuB_2O_4 (I).

The concentration quenching phenomena of Eu^{2+} containing phosphors are interpreted by considering the energy transfer from Eu^{2+} to Eu^{2+} ions on the basis of the Dexter theory, in which the nonradiative process is regarded as being undergone by repeating the energy transfers. Since the 4f–5d transition in Eu^{2+} ions is an allowed one, the transfer will mainly take place via a dipole–dipole interaction. The probability, P, of energy transfer between Eu^{2+} ions by this interaction has been expressed as

$$P_{Eu^{2+}-Eu^{2+}} = (3 \times 10^{12})\frac{P_A}{R^6 \tau_{Eu}} \frac{1}{E^4} \int f_{Eu}(E) F_{Eu}(E)\, dE \quad (2)$$

where P_A is the oscillator strength of the 4f–5d transition in the Eu^{2+} ions, R the distance between the neighboring Eu^{2+} ions (in Å), τ_{Eu} the decay time of the luminescence (in seconds), E the energy involved in the transfer (in electron volts), and $\int f_{Eu}(E) F_{Eu}(E)\, dE$ the overlap between the normalized shapes of the emission and the absorption (reflection) bands of Eu^{2+} ions (in inverse electron volts).

The critical distance, R_c, defined by Blasse[30] is the distance between two luminescent centers, S (sensitizer) and A (activator), at which the probability of transfer from S to A is equal to the probability of radiative emission of S. In eq 2 this means that $P_{Eu-Eu}\tau_{Eu} = 1$, and hence R_c is given as

$$R_c^6 = (3 \times 10^{12})\frac{P_A}{E^4} \int f_{Eu}(E) F_{Eu}(E)\, dE \quad (3)$$

If we substitute in eq 3 $P_A = 0.01$ (the usual value for 4f–5d transitions) and $E = 3.4$ eV (the mean energy around the region in which the emission band overlaps with the reflection band) and we estimate the energy overlap at 1.0 eV^{-1} on $Sr_{0.99}Eu_{0.01}B_2O_4$ (I) from Figure 3 because the emission band completely overlaps with the reflection one, we find $R_c = 25$ Å. Since the mean distance between the neighboring Eu^{2+} ions of EuB_2O_4 is 4.080 Å for six nearest neighbors and 6.632 Å for ten next-nearest neighbors, the probability of $Eu^{2+} \rightarrow Eu^{2+}$ energy transfer is very high and hence the emission from EuB_2O_4 (I) should be very weak. For $Sr_{0.99}Eu_{0.01}B_2O_4$ (I), if the Eu^{2+} ions exist in two types of regions: the Eu^{2+} ions in the first type are dispersed by Sr^{2+} ions at the longer distance than at least 25 Å from the neighboring Eu^{2+} ions while the second type is the region of the cluster formed by a number of Eu^{2+} ions. The Eu^{2+} ions in the former region contribute as the luminescent center, but the concentration quenching effect in the cluster region is expected to be very strong. The energy-level diagram of Eu^{2+} ions in phases I and IV of SrB_2O_4:Eu^{2+} are illustrated in Figure 10. The emission of SrB_2O_4 (I):Eu^{2+} in which many Eu^{2+} ions easily form the cluster should be weak. The energy transfer from Eu^{2+} ions in the former region to Eu^{2+} ions in the cluster region must not entirely contribute to the emission process.

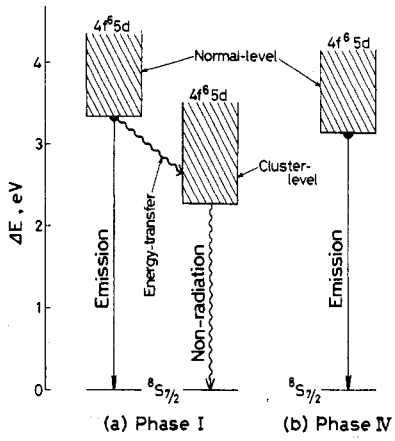

Figure 10. Proposed energy-level diagram of Eu^{2+} ions in phases I and IV of SrB_2O_4:Eu^{2+}. The narrow $4f^7$ level is represented with horizontal lines whereas the broad $4f^65d$ level corresponds to the hatched broad band. The black half-circles are levels of the luminescent center.

The distance R_c can also be estimated from geometrical consideration with help of the following formula:

$$R_c \simeq 2\left(\frac{3V}{4\pi x_c N}\right)^{1/3} \quad (4)^{30}$$

where V is the volume of the unit cell (in $Å^3$), x_c the atom fraction of activator at which the quenching occurs, the so-called critical (optimum) concentration, and N the number of cations which can occupy a unit cell. Accordingly x_c is given as

$$x_c \simeq 6V/\pi N R_c^3 \quad (5)$$

If we substitute in eq 5 $V = 6.589 \times 12.018 \times 4.337$ $Å^3$, $N = 4$, and $R_c = 25$ Å for SrB_2O_4 (I):Eu^{2+}, we find $x_c \simeq 0.01$. This value deviates from the observed one, $x_c \simeq 0.04$ (see Figure 5), and this fact must be due to the formation of clusters. The clusters contribute to decrease the calculated value owing to the increase of the overlap $\int f_{Eu}(E) F_{Eu}(E)\, dE$ between the emission and the reflection spectra while to increasing the observed value because Eu^{2+} ions are concentrated at the limited regions. Consequently the true value must be $0.01 < x_c < 0.04$. The Eu^{2+} ions in SrB_2O_4 (III):Eu^{2+}, which is also the "open" structure, seem almost to behave as well as in SrB_2O_4 (I):Eu^{2+}.

In phase IV of SrB_2O_4:Eu^{2+}, the such cluster region is scarcely formed and each Eu^{2+} ion is considerably isolated from the neighboring Eu^{2+} ions by the BO_4 units, and hence the possibility of $Eu^{2+} \rightarrow Eu^{2+}$ energy transfer must be lower than that of other phases. Consequently the quantum efficiency of SrB_2O_4:Eu^{2+} drastically increases with transformation into phase IV. This agrees with the fact that SrB_4O_7:Eu^{2+}, which consists of a BO_4 network in a similar manner as phase IV and in which the Eu^{2+} ions are completely surrounded by BO_4 units, gives a strong emission compared with other borates, viz., $Sr_3B_2O_6$:Eu^{2+}, $Sr_2B_2O_5$:Eu^{2+}, and SrB_2O_4 (I):Eu^{2+}.[19c]

Conclusion

The phase diagram of EuB_2O_4 consists of the four regions: EuB_2O_4 (I), (III), and (IV) and the decomposed phase $EuB_4O_7 + Eu_2B_2O_5$. Phases I and III and the decomposed phase are antiferromagnetic whereas EuB_2O_4 (IV) has the tendency to be paramagnetic. The high-pressure phases of SrB_2O_4:Eu^{2+} and EuB_2O_4 give the band emissions based on the transition $4f^7$–$4f^65d$ and their emission peak positions shift to long wavelength with changing from phase III to IV because of the

(30) G. Blasse, *Phillips Res. Rep.*, **24**, 131 (1969).
(31) A. L. N. Stevels and A. D. M. Schrama-de Pauw, *J. Electrochem. Soc.*, **123**, 691 (1976).

difference in the coordination of oxygen around Eu^{2+} ions. Also their emission intensities increase with transforming into phase IV. Particularly the quantum efficiency of SrB_2O_4 (IV):Eu^{2+} is about 100 times higher than that of SrB_2O_4 (I):Eu^{2+} under 313-nm excitation. This is due to the fact that a number of Eu^{2+} ions in SrB_2O_4 (IV):Eu^{2+} hardly form the clusters which contribute to the nonradiative process. The luminescence properties of the high-pressure phases of CaB_2O_4:Eu^{2+} correspond to those of the EuB_2O_4 phase pressed out into the grain boundaries of the matrix because of the crystallographic mismatch of Eu^{2+} and Ca^{2+} ions.

Registry No. EuB_2O_4, 38313-81-4; SrB_2O_4, 13703-84-9; CaB_2O_4, 13701-64-9.

Contribution from the Chemical Physics Group, Tata Institute of Fundamental Research, Bombay 400 005, India

Magnetic Susceptibility Study and Ground-State Zero-Field Splitting in Manganese(III) Porphyrins

D. V. BEHERE and SAMARESH MITRA*

Received April 17, 1979

The paper reports results of magnetic measurements on the polycrystalline (4–100 K) and single-crystal (80–300 K) samples of two typical high-spin manganese(III) porphyrins, namely, chloro(tetraphenylporphyrinato)manganese(III) and chloro(tetraphenylporphinato)(pyridine)manganese(III). The experimental data are analyzed in terms of spin-Hamiltonian formalism, which gives an accurate estimate of the zero-field splitting of the ground state of the manganese(III) ion as $D = -2.3$ and -3.0 cm^{-1}, respectively, in the above two compounds. The measurement of single crystal has been found to be particularly informative about the sign and magnitude of D in manganese(III) porphyrins.

Introduction

The magnetic and electronic properties of manganese porphyrins are interesting because of direct and indirect involvement of these molecules in various biological processes.[1-4] A variety of physical studies have been made on manganese(III) porphyrins with a view to understand their electronic structure and other properties. Surprisingly very little attention has been paid to their magnetic susceptibility studies[5] even though it is recognized[6-10] that such study especially on single crystals would be very valuable for understanding ground-state properties of any paramagnetic ion. A survey of existing literature shows that magnetic susceptibility studies on most manganese porphyrins are confined to measurements at room temperature (perhaps just to determine the spin state of the manganese ion); only in a few cases do the measurements extend down to 77 K. There is hardly any report of average magnetic susceptibility study on manganese porphyrins down to liquid-helium temperatures. To our knowledge no single-crystal magnetic susceptibility study on any manganese porphyrin has yet been reported even at room temperature.

In the present paper we report the results of our magnetic susceptibility measurements on polycrystalline (300–4 K) and single-crystal (300–80 K) samples of two benzene-solvated manganese(III) porphyrins, namely, chloro(5,10,15,20-tetraphenylporphinato)manganese(III), ClMnTPP, and chloro-(5,10,15,20-tetraphenylporphinato)(pyridine)manganese(III), Cl(py)MnTPP. Molecular structure of the former is the usual square-pyramidal type with manganese atom being surrounded by the four basal pyrrole nitrogens and an axial chloride ion.[11] In Cl(py)MnTPP hexacoordinated geometry is completed by the pyridine through a long axial Mn–N_{py} bond.[12] The experimental magnetic data on these two related systems are used to deduce zero-field splitting (ZFS) of the ground state. Conventional techniques such as ESR and Mössbauer have not been of any help in determining ZFS in the manganese(III) porphyrins. However values of this important ground-state parameter are known, for comparison, in a few manganese(III) porphyrins by far-infrared spectroscopy.[13]

Experimental Section

ClMnTPP and Cl(py)MnTPP were prepared by literature methods,[14] and their identity was established by elemental analysis[15] and spectra.[16]

Single crystals of ClMnTPP were grown from benzene solution, which readily gave large well-developed tabular single crystals weighing up to 20 mg. These crystals were found to be benzene solvate.[17] Preliminary X-ray studies indicate that the crystals belong to the tetragonal system with $a = 12.9$ Å and $c = 10.2$ Å. Cl(py)MnTPP crystals were grown from a benzene–pyridine solution,[12] which gave large (~12 mg) elongated prismatic crystals. These crystals were also benzene solvate and were established by X-rays to be of the monoclinic system with unit cell data identical with those reported.[12]

Average magnetic susceptibility of the polycrystalline samples was measured between 300 and 4 K by an automatic Oxford Faraday Instrument described in detail elsewhere.[18] The magnetic anisotropy was measured between 300 and 80 K by using the null-deflection

(1) Boucher, L. J. *Coord. Chem. Rev.* **1972**, *7*, 289.
(2) Wang, J. H. *Acc. Chem. Res.* **1970**, *3*, 90.
(3) Olson, J. M. *Science* **1970**, *168*, 438.
(4) Loach, P. A.; Calvin, M. *Biochemistry* **1963**, *2*, 361.
(5) See ref 1 for a listing of the magnetic susceptibility data.
(6) Mitra, S. *Prog. Inorg. Chem.* **1977**, *22*, 309.
(7) Barraclough, C. G.; Martin, R. L.; Mitra, S.; Sherwood, R. C. *J. Chem. Phys.* **1970**, *55*, 1638, 1643.
(8) Venoyama, H.; Lizyka, T.; Morimoto, H.; Kotani, M. *Biochim. Biophys. Acta* **1968**, *160*, 159.
(9) Behere, D. V.; Marathe, V. R.; Mitra, S. *J. Am. Chem. Soc.* **1977**, *99*, 4149.
(10) Ganguli, P.; Marathe, V. R.; Mitra, S. *Inorg. Chem.* **1975**, *14*, 970.
(11) Tulinsky, A.; Chen, B. M. L. *J. Am. Chem. Soc.* **1977**, *99*, 3647.
(12) Kirner, J. F.; Scheidt, W. R. *Inorg. Chem.* **1975**, *14*, 2081.
(13) Brackett, G. C.; Richards, P. L.; Caughey, W. S. *J. Chem. Phys.* **1971**, *54*, 4383.
(14) Adlar, A.; Longo, F. R.; Kampas, F.; Kim. J. *J. Inorg. Nucl. Chem.* **1970**, *32*, 2443.
(15) Microanalysis: Calcd for $TPPMnCl{\cdot}2C_6H_6$: C, 78.3; H, 4.69; N, 6.52. Found: C, 77.5; H, 4.28; N, 6.2. Calcd for $TPPMnCl(py){\cdot}C_6H_6$: C, 76.8; H, 4.57; N, 8.14. Found: C, 76.5; H, 4.6; N, 8.0.
(16) Boucher, L. J. *J. Am. Chem. Soc.* **1970**, *92*, 2725.
(17) Presence of two benzene molecules in the lattice was also confirmed by thermogravimetric analysis.
(18) Mackey, D. J.; Evans, S.; Martin, R. L. *J. Chem. Soc., Dalton Trans.* **1976**, 1515.

0020-1669/80/1319-0992$01.00/0